HHS Public Access

Author manuscript

*IEEE Trans Ultrason Ferroelectr Freq Control*. Author manuscript; available in PMC 2022 March 01.

Published in final edited form as:

*IEEE Trans Ultrason Ferroelectr Freq Control*. 2021 March ; 68(3): 526–537. doi:10.1109/TUFFC.2020.3014183.

# Displacement imaging during focused ultrasound median nerve modulation: A preliminary study in human pain sensation mitigation

**Stephen A. Lee [Student Member, IEEE]**, **Hermes A. S. Kamimura [Member, IEEE]**, **Elisa E. Konofagou [Senior Member, IEEE]**

## Abstract

Focused Ultrasound (FUS)-based viscoelastic imaging techniques using high-frame-rate (HFR) ultrasound to track tissue displacement can be used for mechanistic monitoring of FUS neuromodulation. However, a majority of techniques avoid imaging during the active push transmit (interleaved or post-push acquisitions) to mitigate ultrasound interference, which leads to missing temporal information of ultrasound effects when FUS is being applied. Furthermore, critical for clinical translation, use of both axial steering and real-time (<1s) capabilities for optimizing acoustic parameters for tissue engagement are largely missing. In this study, we describe a method of non-interleaved, single Vantage imaging displacement within an active FUS push with simultaneous axial steering and real-time capabilities using a single ultrasound acquisition machine. Results show that the pulse sequence can track micron-sized displacements using frame rates determined by the calculated time-of-flight (TOF), without interleaving the FUS pulses and imaging acquisition. Decimation by 3–7 frames increases SNR by 15.09±7.03 dB. Benchmarking tests of CUDA-optimized code show increases in processing speed of 35 -and 300-fold in comparison with MATLAB parallel processing GPU and CPU functions, respectively and we can estimate displacement from steered push beams ±10 mm from the geometric focus. Preliminary validation of displacement imaging in humans show that the same driving pressures led to variable nerve engagement, demonstrating important feedback to improve transducer coupling, FUS incident angle, and targeting. Regarding the use of our technique for neuromodulation, we found that FUS altered thermal perception of thermal pain by 0.9643 units of pain ratings in a single trial. Additionally, 5 microns of nerve displacement was shown in on-target vs. off-target sonications. The initial feasibility in healthy volunteers warrants further study for potential clinical translation of FUS for pain suppression.

### Keywords

CUDA; elastography; focused ultrasound; GPU-accelerated; humans; pain; neuromodulation

## I. Introduction

NEUROMODULATORY effects of ultrasound on electrically excitable tissues have been widely observed [1]–[3]. Ultrasound has been proven capable of modulating ion channel, peripheral nerve, and brain activity in a multitude of *in vitro, ex vivo, and in vivo* studies [4]–[12]. In specifically the peripheral nerves, both pulsed ultrasound in the kilohertz (kHz)

range [13], [14] and continuous wave (CW) ultrasound in the megahertz (MHz) range [10] have been reported to lead to elicited responses in both nerve and muscle recordings. Though a common mechanism has not been discovered, our previous studies using CW ultrasound, show neuromodulation activity has a higher probability of activation using short duration, high intensity pulses [15]. These reports indicate that the mechanism of ultrasound neuromodulation in the peripheral nervous system most likely involves acoustic radiation forces.

Focused ultrasound (FUS) provides an attractive method for non-invasive therapeutics and neuromodulation due to its high spatial resolution and deep penetration. It is for this reason that FUS has been approved in the clinic for treatment of essential tremors [16]. Moreover, transcranial FUS for neuromodulation in humans has shown various changes in perception of touch and vision. Legon et al. 2014 [17] used low intensity pulsed ultrasound in the brain to change thresholds of air puffs and two-point discrimination behavioral tests. In 2015, Lee et al. demonstrated that transcranial FUS can also elicit sensory perceptions in humans [18]. Lastly, Dickey et al. 2012 [19] was able to, in a similar fashion to Gavrilov [20] in 1984, stimulate the skin receptive fields of the peripheral nervous system (PNS). In our previous studies in *in vivo* and *ex vivo* mice preparations [15], [21], there is evidence that different nerve fibers, including C-fibers which are pain transducing neurons, can be preferentially stimulated using FUS. To translate these findings into a human model, not just accurate and reliable targeting is needed, but also real-time feedback of where and what intensity of the FUS is delivered to the nerve.

Current methods of FUS targeting largely rely upon MRI-based methods or B-mode ultrasound-guided imaging [22]–[24]. MRI-guided FUS (MRIgFUS) is reliable, albeit a costly modality, requiring compliant transducers and equipment to minimize interaction with the magnetic fields. Though commercially available, MRI-compatible transducers heavily restrict what experiments can be performed inside the coil. On the other hand, ultrasound-guided (B-mode) FUS does not require specialized equipment. However, B-mode imaging and identification of tissue structures based on speckle patterns typically require experienced sonographers and only provide anatomical information but not targeting confirmation. Neither of these techniques are capable of providing real-time feedback and monitoring on where and to what extent ultrasound engages the targeted tissues. Current MR-based imaging techniques can measure temperature or displacement using interleaved FUS pulses [25], though the displacements reported are an effective average displacements and may not reflect the true displacement, whereas interleaved and non-interleaved ultrasound-based cross-correlation techniques can measure displacements down to the theoretical Cramer-Rao lower bound [26]. Considerable advances in MRI-based Elastography and ARFI techniques enable detection of micron displacements within FUS pulses [27]–[30]. However, to acquire higher frame rates, event locking MRI acquisitions to the FUS pulse requires multiple sonications to acquire the full temporal displacement profile [25]. Because neuromodulatory effects are unique to a specific FUS pulse, it would be more informative to have both spatial and temporal displacement profiles for a single FUS pulse. Frame rates in MR-ARFI may range from 0.5 [29] to 1 Hz [28] whereas ultrasound elastography can achieve frame rates thousands of times higher. Therefore, a non-invasive ultrasound-based technique for accurate

real-time monitoring and targeting of the actual FUS beam used in neuromodulation is needed.

Ultrasound imaging techniques for tissue elasticity measurement have had success in various medical applications. These methods usually depend upon accurate displacement estimation of tissue between sequential ultrasound frames [31]. Techniques such as acoustic radiation force imaging (ARFI), shear wave imaging, and harmonic motion imaging (HMI), utilize radiation forces to generate local displacements within the tissue, palpating non-invasively using ultrasound [32], [33]. Tissue motion caused by this radiation force can be tracked using cross-correlation algorithms [34]. Additionally, using 2D or 3D probes for ARFI, the localized response in the tissue can be tracked both spatially and temporally [35]. Feasibility of ARFI has been demonstrated in numerous studies and in clinical applications such as breast, abdominal muscle, heart, liver, and colon imaging [36]–[38]. Acoustic radiation force can also be used to image lesions in the tissue where conventional ultrasound imaging has poor visualization [39], [40]. Additionally, real-time ARFI has been applied to guide surgical procedures and high intensity focused ultrasound (HIFU) ablation [41], [42]. Since we hypothesize radiation force is involved in the mechanism of FUS neuromodulation, we may be able to take advantage of conventional elastography imaging techniques to monitor and target acoustic radiation force generated by FUS pushes. We have previously demonstrated this technique in mice for mechanistic studies, relating displacement to the amount of neuromodulation of the sciatic nerve [43].

As previously mentioned, conventional acoustic radiation force imaging techniques do not image within the push pulse. For systems that use a single transducer to push and image, the contribution of all the elements are needed to remotely palpate the tissue, thus imaging must occur after the acoustic radiation force delivery. Systems using confocal arrangements of two transducers experience interference between the push transducer and the imaging transducer bandwidth. Current, monitoring techniques implement filtering and/or coded excitation to avoid this interference [40], [44]. However, pulse length for therapy and lesion monitoring indicated in these studies are on orders of seconds as opposed to <2 ms for neuromodulation. Methods, such as Supersonic Shear Imaging, interleave imaging and push pulses at multiple focal depths [45]. But interleaving imaging between pushes limits the amount of displacement and thus may change neuromodulatory effects. Therefore, we present a technique for HFR displacement tracking of the FUS beam using two confocal transducers and a single ultrasound data acquisition (DAQ) Vantage system for real-time targeting and monitoring of the median nerve. Lastly, we use this method to acquire preliminary evidence for FUS-modulated thermal sensations in humans.

## II. Materials and Methods

### A. Displacement Experimental Setup

The DAQ system includes one 256 channel Vantage research platform with the HIFU option (Verasonics, Kirkland, WA, USA) coupled with the extended burst power supply Fig. 1. The power supply enables driving multiple cycle transmits. Half of the 256 connectors is connected to a 104 element P12–5 Phased Array transducer (ATL Philips, Bothell, WA, USA) for simultaneous imaging and displacement tracking. The other 128 elements were

connected to a RF matching box for a 4 element, 1.1 MHz FUS transducer (SonicConcepts, Bothell, WA, USA). A customized matching box directs power from the 64 channels in the right connector to the 4 element annular rings (16 mm width) with area (450, 550, 650, and 70 $mm^2$); each annular element is driven by 16 channels. The FUS transducer has an active diameter of 64 mm with a 40 mm opening where the imaging transducer was placed through (Fig. 1a). The attached coupling cone opening is 77 mm in diameter with two tubes for degassing the water in the transducer cone or inflation/deflation of the membrane. The focus of the FUS transducer (0.5 × 15 mm) was aligned using a custom 3D printed mold so that the plane of the imaging transducer was centered at 30 mm in depth. The FUS frequency and size of the focal region were chosen to optimize adequate radiation pressure, relative to the focal size-to-nerve ratio. The focus encompasses the nerve diameter completely in the axial direction and 20% in the lateral direction. RF signals acquired for HFR displacement tracking were processed in real-time using a GPU CUDA-accelerated delay-and-sum (DAS) beamforming and 1D cross correlation algorithm [46].

Compounded plane wave images were used for initial targeting of the nerve. We used 5 angles (±9°) and 1 transmit-receive operation per angle to generate a B-mode image (Fig 1b) with the focus at 30 mm. Beamformed RF data was fed into a normalized cross-correlation algorithm [46] to generate displacement maps of FUS pushes overlaid onto B-mode images. A a 95% overlap and a window size of 12.25 mm was used to track displacements in the raw RF data. Derated peak negative pressures used in phantoms were under 10.9 MPa peak negative pressure (MI = 10.1, 72.3 $W/cm^2$ $I_{SPPA}$) and under 7.9 MPa (MI = 7.5, 29.4 $W/cm^2$ $I_{SPPA}$) in humans.

### B. Simultaneous Single-system FUS Displacement Tracking Pulse Sequence

Currently, the ultrasound DAQ system has not been configured for within-pulse imaging across two transducers without interleaving sequences. Therefore, a strategy for continuous imaging and monitoring must be developed to allow displacement tracking within the FUS push. Simultaneous imaging of FUS pushes requires customized ultrasonic parameters for each transducer. A 1.5 cycle plane wave emission was programmed for all 128 channels connected to the P12–5. In order to utilize both transducers without interleaving, the pulse duration of the FUS transducer was set to a proportion of the total time-of-flight (TOF) for a wave to travel from the imaging transducer face to a scatterer at the edge of the imaging window and back. Therefore, to generate an image at 41 mm from the transducer face (aperture of 9.94 mm), the TOF (71 $\mu s$) sets the extended FUS burst to be an integer multiple of the TOF. To reach a burst pulse duration of 5 ms, matching pulse durations seen in previous PNS neuromodulation studies, 70 bursts of ultrasound without interval between pulse trains were transmitted during the FUS push. The 71 $\mu s$ bursts are programmed into the right 128 channels of the DAQ which are used to drive all four annular elements.

Fig. 2 shows the pulse sequence of the proposed technique. The FUS push is shown in blue and the imaging pulse in black. The total frame rate of the technique is also depth dependent; for a depth of 41 mm, the frame-rate is 14 kHz. Hydrophone measurements of the FUS and imaging transducers in free field (HGL-200 & HFO-660, Onda Corp, Sunnyvale, CA) is shown in Fig. 2 middle. Hydrophone measurements reveal a 17 $\mu s$ gap

between subsequent FUS bursts. This was caused by a combination of electronic processing time and actuation time of the elements. The processing sequence is defined in Fig. 2. After stacking and transferring all RF imaging frames, the RF data is beamformed using a CUDA-accelerated (CUDA version 9.1) conventional DAS beamforming. The parallel calculations were performed using a GPU (Tesla k40c, Nvidia, Santa Clara, CA, USA) with 1024 threads and 3 dimensional indexing. Beamformed RF data was filtered using a comb notch filter at all the fundamental (1.1 MHz) and harmonic frequencies (2.2 – 12.1 MHz) of the FUS transducer found within the P12–5 bandwidth. Harmonic Frequencies within the 60% bandwidth of the P12–5 were not applied in order to maximize signal-to-noise (SNR) of the echoes. Second order Butterworth notch bandwidths were set to 50% of the notch frequencies and filter coefficients were calculated before the imaging sequence so that in-sequence calculations would be devoted to beamforming and cross correlation. Displacement calculations were performed by 1D cross-correlation with a 95% overlap and a window size of 12.25 mm [43]. Displacement maps were smoothed using a 2D median filter of 0.2% of the reconstruction grid. Displacements were then overlaid onto the filtered B-mode images after calculation of all frames and displayed in real-time.

### C. CUDA benchmarking

CUDA DAS beamforming was implemented through MATLAB GPU kernels. Variables used to beamform in real-time were stored in the shared memory on the GPU before imaging execution. All delays were calculated and summed up for each pixel in the desired linear interpolation grid. 3D indexing was used for each calculation in time (frames) and spatial (depth and lateral) points on 1024 threads divided into 3 blocks. The kernel grid size was determined as a proportion of the reconstructed frames and spatial grid. Lastly, beamforming operation was performed by passing the raw RF data as a singular vector array.

For benchmarking GPU performance, MATLAB's GPU parallel computing toolbox, CPU multi-core (parfor), and CPU single-core operations were used as comparisons. DAS using MATLAB's toolbox was performed by pre-allocating interpolated RF samples and pre-defining forwards, backwards, and compounding delay arrays on the GPU. During imaging operation, RF data was then beamformed by linearly interpolating the RF data onto pre-indexed and pre-defined delays. The same calculations performed in C++ were separately performed on a single CPU and using parfor loops using 12 workers on two CPU cores. Two sets of analysis were performed using a sample acquired RF data of size 1152 (samples) x 104 (elements). Computational time was calculated by increasing the number of samples or increasing the interpolation grid size and resolution. Benchmarking code can be made provided upon request.

### D. Frame decimation

The accuracy and dynamic range of displacement tracking a 1.1 MHz ARF push is diminished. Therefore, to increase sensitivity and accuracy for real-time, intraprocedural targeting and monitoring, we can either increase transducer driving power or remove and decimate subsequent frames so that interframe displacement increases without changes to overall cumulative displacement. For every displacement map, RF of dimension 104 elements x 1152 samples were stacked by the number of frames into a larger 2D array (104

× 80640 for a 70 frames) and acquired at the highest frame-rate required to image at a specific depth. To emphasize larger displacement estimates, we can down-sample a percentage of frames and feed the resulting beamformed RF into the displacement estimation algorithm. In our optimization, we decimated by a factor of 0, 3, 5, 7, and 9 (i.e., removing zero, every 3rd, 5th, 7th, or 9th frame). Therefore, for a 5 ms FUS pulse, the received 70 frames would be reduced to 23 frames after decimation by 3, allowing larger displacement measurements between subsequent frames. Afterwards, SNR was calculated on the displacement signals for every decimation factor.

### E. Sample preparation

A polyacrylamide tissue-mimicking phantom with 4% agar powder (Sigma-Aldrich, St. Louis, MO) as a scattering particle [47] was used to validate the displacement imaging. The phantom has an elastic modulus of 10 kPa, which was determined using the methodology described by Han et al. 2015 [48].

### F. Human subject preparation

All human subjects (n=5) were recruited acquired in accordance with the 2013 Declaration of Helsinki. Ethical oversight and approval for this study was provided by the Institutional Review Board of Columbia University under protocol AAAR4475. Human subjects were seated comfortably with their forearm resting in a mechanical and movable cuff. The forearm was placed as to not introduce any physical shifting during the experiment. Degassed ultrasound gel was used to couple the transducer system bladder to the forearm. Compound B-mode imaging was used to initially place the therapeutic transducer focus on the median nerve.

Heat stimulation pulses were delivered to the C6 dermatome of the right arm (n = 1) using a custom-built thermofoil device. This initial feasibility study was set so that the FUS was delivered exactly when the heat signal was applied to the palm. FUS sonications (on target and off target) were randomized within the 14 heat pulses delivered and the subject was asked to rate the intensity of the thermal stimulus using the Wong-Baker scale [49]. Though the scale ranges from 0 to 10, we kept thermal stimulation ratings in the range of 3 to 6.

### G. Statistical analysis

All data was acquired in accordance with the Columbia University Institutional Review Board regarding patient data collection. Statistical testing was performed in Prism 8 (Graphpad, San Diego, CA) using a non-parametric Mann-Whitney test to test for differences between ratings given concurrently with FUS or sham sonication.

## III. Results

### A. Signal-to-Noise Optimization

The imaging technique, using a 5 ms pulse sequence, in Fig. 2 was optimized by calculating SNR during the FUS pulse in a gelatin tissue-mimicking phantom for decimated displacement estimation (0, 3, 5, 7, and 9 frames) at varying levels of focal pressures (Fig. 3). The displacement maps shown are 0.16, 0.40, and 0.55 ms after triggering the FUS pulse.

Displacements illustrate the ellipsoidal shape of the FUS beam but with increased lateral extent due to decimation. All calculations were performed using the ROI defined in Fig. 3 (top), placed at the center of the transducer focus (30 mm). Ten pressure levels, 5 realizations each, were used to acquire raw RF data using our technique. Post-hoc, frames were decimated by a factor ranging from 0 to 9 frames and the resulting displacement for each realization was estimated using normalized cross correlation. The resulting displacement maps (Fig. 3 top) show larger interframe displacement values and illustrate the ellipsoidal focus better as more decimation is used. The associated interframe displacement traces are shown for a 5 ms FUS pulse in Fig. 3 bottom. Decimated displacements have fewer time-points within the FUS pulse but have larger displacement values. Lastly, the SNR was calculated within the pulse using the following equation [50], [51]:

$$SNR = \frac{\mu}{\sigma} \quad (1)$$

where $\mu$ is the mean displacement and $\sigma$ is the variance across all realizations within the ROI. SNR was calculated for displacement values only within the FUS pulse. Results show that, for a 5 ms pulse, decimation by 7 frames had the largest increase in SNR by 15.09 ± 7.03 dB compared to no zero decimation across all pressure levels. As such, displacement SNR increases with pressure, peaking at 5.7 MPa until the noise from FUS harmonics severely impedes both B-mode quality and the estimated displacement. Therefore, trade-offs between maximized SNR and number of frames within the FUS pulse indicate that optimal decimation rates should range from 3 to 7 frames. Thus, for the following study, all RF data was decimated by 5 frames before displacement estimation.

## B. GPU Benchmarking

GPU parallelization of DAS beamforming using CUDA programming was compared to GPU parallelization using MATLAB's parallel computing toolbox, CPU parallelization (12 workers) over 2 cores, and CPU calculation on one core. Fig. 4 shows computation time over number of samples beamformed. Averages over 3 realizations at increasing number of RF samples show similar computation time for both GPU methods until $10^5$ samples. At $>10^5$ samples, CUDA GPU performance shows increasing computational speedup up to 35 times the MATLAB GPU computational time. CUDA GPU maintains consistent speed up over CPU and parallel CPU by 300 and 60 times, respectively. Lastly, CUDA performs under real-time criteria up to $10^{5.6}$ samples.

The same computational time comparisons were performed for different DAS interpolated grid size resolutions (1, 0.5, 0.25, 0.125) for 70 frames of 1152 RF samples of base grid size of 60 × 512 pixels. Fig. 5 shows CUDA DAS performs well compared to all other computational frameworks. The MATLAB parallel toolbox and CUDA kernel performance was similar until (240×2048 pixels) grid sizes. The CUDA kernel was not able to perform in real-time at grid sizes 480×4096 pixels and above. Benchmarking results also show considerable speedup over CPU calculations.

### C. Axial Displacement Focusing

The FUS beam was electronically focused in the axial direction by calculating delays for each of the 4 annular ultrasonic elements so that the focal point is moved in the axial direction. Variations in the beam-shape occurs due to the changes in the f-number. Hydrophone measurements of the beam profile in free-field show axial focusing capabilities up to ±10 mm relative to the geometric focal center. Axial focusing less than ±5 mm leads to −3 dB drop off in pressure and greater than ±5 mm shows greater drop off up to −6 dB. Displacement maps in a homogeneous phantom were generated for each focal depth. Fig. 6 shows relevant focal displacements at −5, 0, 5, and 10 mm focal depths relative to the geometric center at the same time point. The figure illustrates maps showing maximum interframe displacement, corresponding to the first frames of FUS sonication (representative displacement trace is shown in Fig. 3). The ellipsoidal shape of the focus can best be visualized at ±5 mm. At larger axial focusing positions, the displacements succumb to unfilterable FUS interference noise from overlapping FUS and imaging beams.

### D. Human median nerve targeting

In Fig. 7 we implemented the pulse sequence to facilitate targeting for human nerve neuromodulation in healthy subjects (n = 5). Nerve displacements up to 1 $\mu m$, overlapping with the FUS focus, are shown in the second frame. Upwards displacement/relaxation begins at 32 mm in frame 3 and propagates outwards in frame 4. Interestingly, there are visible differences nerve displacement versus muscle (above 29 mm). This technique was used to first target the nerve, ensuring maximum FUS delivery to the nerve. Varying levels of displacement for the five subjects were measured using a 5 ms FUS pulse (5.6 MPa and 7.9 MPa peak rarefactional pressure). Mean displacement values at the center of the nerve (black ROI) from 7 FUS pulses are reported in Table I. Though the focal pressure output from the transducer was the same from subject to subject, the amount of displacement varied from 10 to 30 microns in peak cumulative displacement. After targeting validation, displacement images were used to monitor neuromodulation.

A neuromodulation experiment was conducted to validate the technique in a sensory neuromodulation experiment. Fifteen 2 second thermal pulses were delivered to the C6 dermatome of the human palm at a random interval between 3 and 4 minutes and a subject (n = 1) was asked to rate the intensity of the pulse based on the Wong-Baker scale [49]. FUS (7.9 MPa rarefactional pressure) and sham (no FUS and off target FUS) stimulations were randomized among the 15 heat pulses delivered in a single trial. Displacement imaging allowed monitoring of all FUS pulses and measurement of displacement at the nerve. Fig. 8 shows one frame of the supplementary video 1, indicating FUS engagement of the median nerve. To investigate acute effects of FUS on sensory perception, a pulse duration of 5 ms was chosen to ensure FUS was applied during sensory stimulus conduction; based on the average conduction velocity in a healthy human subject [52] and the approximate distance of the FUS focus to the thermal stimulus (approximately 5 – 6 cm). Both interframe and cumulative displacement were estimated during the FUS pulse transmission at the peak of temperature delivery. For this particular subject, the peak interframe and cumulative displacements were estimated at the center of the nerve (black ROI) during neuromodulation was 5.1 ± 0.7 and 40.7 ± 7.4 microns, respectively. The maximum interframe displacement

was achieved at the beginning of the pulse and the peak cumulative displacement was acquired at the end of the FUS pulse. Sources of error in the displacement curve may be due to slight movement in the subjects' arm during the procedure. Preliminary data indicates that FUS may change subjective thermal perception by modulating the median nerve during heat stimulation. Fig. 9 shows ratings from heat stimuli with FUS vs sham. A 0.9643 pain rating unit decrease, without significance, was found in FUS sonications vs. sham stimulations ($p = 0.0547$; two-tailed unpaired Mann-Whitney test) where lower ratings were indicated for lower needle-like thermal pain.

For further validation of our technique to neuromodulation, we note differences between FUS delivery when FUS is applied directly to the nerve vs off-target. Fig. 10 illustrates a representative displacement image when the focus was off the median nerve (white outline). FUS displacement still appears at the focus of the transducer, however the nerve was positioned 5 mm away. As a result, the displacement at the center of the nerve (black ROI) had a peak cumulative displacement of 3.2±1.7 microns when the focus was off-target. Moreover, the peak interframe displacement was 1.7±0.3 microns at the end of the FUS pulse rather than the beginning as in Fig. 8 with a 5 $\mu m$ difference in peaks. Finally, the thermal stimulations which were off-target had an average rating of 1 higher than when FUS was acting on the nerve directly ($p = 0.4524$; two-tailed unpaired Mann-Whitney test).

## IV. Discussion

Using a confocally aligned imaging and FUS transducer, we can perform real-time displacement tracking, mediated by CUDA-accelerated DAS, and axial focal steering using a single ultrasound DAQ system without interleaving. Half of the channels can be used to drive the FUS-guided system with simultaneous custom waveforms programmed for imaging on half the channels and FUS on the other. A major advantage of using this technique, is the ability to perform RF stacking and displacement tracking in real-time.

Using the Cramer-Rao lower bound [26] for a SNR of 30 dB, a correlation coefficient of 0.98, and a window length of 11.25 $\mu s$ our technique can ideally achieve displacements above 0.6711 $\mu m$ where they succumb to jitter. Though, our transducer can achieve ±10 mm axial steering of the FUS focus, there is a drop off in tracked displacement. This phenomenon is especially apparent at lower positions, where these low pressure pushes are below the noise floor. However, the ±5 mm range is more than adequate for targeting the median nerve in the human arm and accounting for small movements, limiting off-target effects. In the distal half of the forearm, the variation in depth of the median nerve is well within the range of 5 mm. Furthermore, since active compounded B-mode imaging is continuously used between displacement mapping sonications, we can actively account for any movement during the entire procedure.

Benchmarking clearly shows the advantages of parallel GPU computing for conventional DAS compared to CPU calculations. However, the advantage of CUDA beamforming over using GPU matrices in the MATLAB toolbox are not as easily distinguishable. Computational speedup only occurs at high data volumes and for displacement mapping, higher resolution interpolation grids increase SNR of displacements and may benefit from

CUDA operation. This deviation may be due to how CUDA-written programs efficiently use shared memory whereas the MATLAB parallel computing toolbox does not. Other techniques, such as Doppler functional UltraSound (fUS) would also benefit from utilizing CUDA kernels as compounding more than 200 frames can become computationally intensive. Not included in the above benchmarking analysis is the acceleration of the initialization of the imaging sequence. Because the MATLAB toolbox technique involves pre-indexing and delay calculation, initialization of scripts using large data volumes may take minutes to initialize. However, CUDA calculation is performed in real-time, leading to less wait time and faster in-procedure operation. On the other hand, as of now, the proposed technique achieves real-time specifications and CUDA beamforming may benefit from calculating delays before initialization instead of during acquisition so that during imaging operation, other computationally intensive operations may take priority, speeding up the technique. This technique is feasible to implement in other more conventional ultrasound systems if an external FUS transducer is used or a custom device to allocate channels to a FUS transducer and imaging transducer, given the sufficient frame rates (above 10 kHz) and output power (0.5 to 1 MPa) can be achieved. Lower number of imaging channels will not impede displacement mapping, as probes such as the P4–2 (64 channels) can be used to track tissue motion [48]. Lastly, the imaging frequency must be selected so as to minimize the overlap of the FUS transducer center and harmonic frequencies.

We demonstrate our technique's capability to facilitate targeting (n = 5) of the median nerve in and neuromodulation (n = 1) in healthy human subjects. Displacement maps show that the intensity of the displacement increases as the pressure is increased. Due to the heterogeneity of the forearm and boundary effects between muscle, connective tissue, and nerve fibers, the displacement map does not necessarily follow the expected ellipsoidal focus geometry. Additionally, the variance within a single subject was consistent between FUS pulses (max standard deviation of 10.7 microns). However, our technique reveals that same output pressures do not necessarily translate to the same FUS modulation efficiency (nerve displacement) between subjects. We measured 50 $\mu$m nerve displacement from a 5.6 MPa, 5 ms pulse in 1 subject but 18 $\mu$m in another from the same pulse parameters. This can be due to a number of factors: location of the transducer on the forearm, the incident angle to the skin, tissue properties, and how well coupled the transducer system is to the skin. Finally, we present a preliminary findings showing FUS effects on thermal pain perception. Results show that thermal pulses with coincident FUS sonication had lower thermal ratings than sham pulses. Moreover, pulses that were off-target to the nerve had a higher rating than when the focus was positioned at the center of the nerve. Displacement maps show that displacement characteristics are vastly different between on- and off-target pulses. The peak of interframe displacement was near the beginning of the pulse for on-target versus the end of the pulse for off-target (Fig. 10). FUS was capable of suppressing pain signals only when directly targeted to the nerve trunk. This effect could be explained by either the generation of afferent signals at the nerve trunk, generating a masking effect of pain, changing how the subject perceives pain or, most likely, by the direct suppression or interruption of signals by FUS at a more proximal portion of the nerve trunk. The masking effect is unlikely to occur because the sonication using the parameters used in this study without any other stimuli did not generate any sensory response itself. Future studies will explore this hypothesis, for

example, targeting receptive fields at the skin in order to generate tactile sensations during a concurrent pain task.

Limitations of operating at 1.1 MHz as opposed to higher frequencies, includes lower tissue displacements as the tissue absorption and acoustic radiation force decrease with frequency. Interleaving transmits would lower the amplitude of displacements further, thus simultaneous imaging within the pulse is essential. The trade-off of this technique is the interference from the FUS transducer. Ideally, the transducer bandwidths should be separated as far as possible to reduce the interference, but the depth penetration limits the range of frequencies. Additional filtering can minimize interference, but an inherent smoothing of the RF data is inevitable. Nonetheless, we can adapt this single DAQ method to other elastography techniques such as harmonic motion imaging (HMI) by amplitude modulating the HIFU [42]. As noted before, hydrophone measurements show that we emitted a pseudo-CW push due to electronic actuation of elements. The effect of this timing on displacement has yet to be determined. However, more complex coded excitations can be developed to achieve true CW such as the ones presented by Tiran et al. 2015 [53].

In ultrasound neuromodulation literature thus far, proper targeting is an often overlooked aspect of experimental design, but having real-time feedback and confirmation of targeting can lead to more conclusive results. Crucially, we found that transducer driving pressure does not necessarily lead to reproducible therapeutic levels subject to subject, providing an explanation for the wide variety of US pressures reported in neuromodulation, i.e., 1.8 MPa, 3.2 MPa, or even 50 MPa to achieve an action potential [54]. Displacement imaging reveals real-time feedback on how much FUS is engaging the nerve, which may vary subject to subject or in the same subject depending on the coupling condition (i.e. coupling gel, incidence angle). We show that transducer focal pressure may not be a valid indication of FUS nerve modulation efficacy; using displacement imaging may facilitate comparison to other reports of FUS neuromodulation. Furthermore, the ability to focus-shift adds to the ability to modify targeting during the procedure in remedy of poor coupling, movement artifacts, and off-target effects. Lastly, we have shown that variation can be detected and imaged with this technique which may play an important role in further characterizing the mechanism of FUS neuromodulation.

## V. Conclusion

By deriving a new pulse sequence and hardware combination to simultaneously drive a FUS and imaging transducer with a single ultrasound DAQ system, we have shown in this article that tracking displacements within the FUS pulse for targeting and monitoring can be accomplished. The pulse sequence and frame-rate were experimentally optimized using a homogeneous tissue-mimicking phantom and applied to *in vivo* human median nerve stimulation. Furthermore, the technique is able to operate in real-time and account for shifts in targeting using axial beam steering. We found that the micron displacements in the nerve were able to confirm FUS delivery. Lastly, the imaging technique presented herein was successfully validated in an experiment demonstrating FUS effects on thermal perception where the subject experienced a 0.9643 pain rating unit decrease in the needle-like pain sensation. Moreover, our technique can validate on- and off-targeting of the nerve indicating

5-micron differences at the transducer driving pressures explored in this study. The imaging technique developed here is not restricted to the tissues validated in this article, but can be applied to any ultrasound-accessible soft tissue found elsewhere in the body, such as the brain. Furthermore, current studies would benefit from a method that allows for real-time targeting, allowing for greater confidence in the results of FUS mechanistic studies.

## Supplementary Material

Refer to Web version on PubMed Central for supplementary material.

## Acknowledgments

This work was supported by the Defense Advanced Research Projects Agency (DARPA) Biological Technologies Office (BTO) Electrical Prescriptions (ElectRx) (Grant/Contract No. DARPA HR0011-15-2-0054), the National Institute of Biomedical Imaging and Bioengineering of the National Institutes of Health under Award Number R01EB027576, Sound-Stim Inc, and Google X.

## Biography

**Stephen A. Lee** received the bachelor's degree from the University of North Carolina at Chapel Hill, Chapel Hill, NC, USA in 2015, and the Master's of Science degree from Columbia University, New York, NY, USA in 2018. In 2016, he enrolled in the M.S./Ph.D. Program with the Department of Biomedical Engineering, Columbia University, New York, NY, USA where he is currently working towards his Ph.D. His current research interests include studying the mechanism of ultrasound neuromodulation and how ultrasound imaging and simulation techniques can be used understand this phenomenon. In 2019, he was the recipient of the IEEE IUS student paper competition award.

**Hermes A.S. Kamimura** (Member, IEEE) received the B.S. degree in medical physics and the M.S. and Ph.D. degrees in physics applied to medicine and biology from the University of São Paulo, Ribeirão Preto, Brazil, in 2008, 2011, and 2016, respectively. He conducted research projects in therapeutic and ultrasound imaging at Mayo Clinic, Rochester, MN, USA, in 2010, and also at Columbia University, New York, NY, USA, in 2014, in student exchange programs. He was a Postdoctoral Research Scientist with French Alternative Energies and Atomic Energy Commission (CEA), Gif-sur-Yvette, France, and also with Columbia University, where he is currently an Associate Research Scientist. His research interests include harmonic motion imaging and therapeutic ultrasound spanning both

ultrasound neuromodulation and ultrasound mediated bloodbrain barrier disruption for targeted brain drug delivery. Dr. Kamimura is a member of the Brazilian Physical Society and Brazilian Society of Biomedical Engineering. He was a recipient of the Outstanding Reviewer Award for Physics in Medicine and Biology, IOP Publishing in 2018, and the Best Ph.D. Dissertation Award in the field of medical physics in 2016 by the Brazilian Physical Society. He serves as a Topic Editor for Frontiers in Physics and Frontiers in Physiology.

**Elisa E. Konofagou** (S98A99M03) is currently the Robert and Margaret Hariri Professor of biomedical engineering and a Professor of radiology as well as the Director of the Ultrasound and Elasticity Imaging Laboratory with the Biomedical Engineering Department, Columbia University, New York, NY, USA. She has co-authored over 170 peer-reviewed journal articles. Her current research interests include the development of novel elasticity imaging techniques and therapeutic ultrasound methods and more notably, myocardial elastography, electromechanical and pulse wave imaging, harmonic motion imaging, focused ultrasound therapy, and drug delivery in the brain, with several clinical collaborations in the Columbia Presbyterian Medical Center, New York, NY, USA, and elsewhere. Prof. Konofagou was a recipient of awards, such as the CAREER Award from the National Science Foundation and the Nagy Award from the National Institutes of Health as well as others from the American Heart Association, the Acoustical Society of America, the American Institute of Ultrasound in Medicine, the Wallace H. Coulter Foundation, the Bodossaki Foundation, the Society of Photo-Optical Instrumentation Engineers, and the Radiological Society of North America. She is a Technical Committee Member of the Acoustical Society of America, the International Society of Therapeutic Ultrasound, the IEEE Engineering in Medicine and Biology Conference, the IEEE International Ultrasonics Symposium, and the American Association of Physicists in Medicine. She serves as an Associate Editor for the IEEE Transactions on ultrasonics, ferroelectrics, and frequency control, Ultrasonic Imaging, and Medical Physics.

## References

[1]. Naor O, Krupa S, and Shoham S, “Ultrasonic neuromodulation,” Journal of Neural Engineering, vol. 13, no. 3, p. 031003, 5 2016. [PubMed: 27153566]

[2]. Fomenko A, Neudorfer C, Dallapiazza RF, Kalia SK, and Lozano AM, “Low-intensity ultrasound neuromodulation: An overview of mechanisms and emerging human applications,” Brain Stimulation, vol. 11, no. 6, pp. 1209–1217, 2018. [PubMed: 30166265]

[3]. Pasquinelli C, Hanson LG, Siebner HR, Lee HJ, and Thielscher A, “Safety of transcranial focused ultrasound stimulation: A systematic review of the state of knowledge from both human and animal studies,” Brain Stimulation, 2019.

[4]. King RL, Brown JR, Newsome WT, and Pauly KB, “Effective parameters for ultrasound-induced in vivo neurostimulation,” Ultrasound in Medicine and Biology, vol. 39, no. 2, pp. 312–331, 2013. [PubMed: 23219040]

[5]. Baek H, Pahk KJ, and Kim H, “A review of low-intensity focused ultrasound for neuromodulation,” Biomedical Engineering Letters, vol. 7, no. 2, pp. 135–142, 2017. [PubMed: 30603160]

[6]. Kubanek J, Shi J, Marsh J, Chen D, Deng C, and Cui J, “Ultrasound modulates ion channel currents,” Scientific Reports, vol. 6, p. 24170, 2016. [PubMed: 27112990]

[7]. Kamimura HAS, Wang S, Chen H, Wang Q, Aurup C, Acosta C, Carneiro AAO, and Konofagou EE, “Focused ultrasound neuromodulation of cortical and subcortical brain structures using 1.9 MHz,” Medical Physics, vol. 43, no. 10, pp. 5730–5735, 9 2016. [PubMed: 27782686]

[8]. Tufail Y, Matyushov A, Baldwin N, Tauchmann ML, Georges J, Yoshihiro A, Tillery SI, and Tyler WJ, “Transcranial Pulsed Ultrasound Stimulates Intact Brain Circuits,” Neuron, vol. 66, no. 5, pp. 681–694, 2010. [PubMed: 20547127]

[9]. Lee W, Kim H-C, Jung Y, Chung YA, Song I-U, Lee J-H, and Yoo S-S, “Transcranial focused ultrasound stimulation of human primary visual cortex,” Scientific Reports, vol. 6, no. 1, p. 34026, 2016. [PubMed: 27658372]

[10]. Lele PP, “Effects of focused ultrasonic radiation on peripheral nerve, with observations on local heating,” Experimental Neurology, vol. 8, no. 1, pp. 47–83, 1963.

[11]. Tyler WJ, Tufail Y, Finsterwald M, Tauchmann ML, Olson EJ, and Majestic C, “Remote excitation of neuronal circuits using low-intensity, low-frequency ultrasound,” PLoS ONE, vol. 3, no. 10, 2008.

[12]. Kamimura HAS, Conti A, Toschi N, and Konofagou EE, “Ultrasound neuromodulation: Mechanisms and the potential of multimodal stimulation for neuronal function assessment,” Frontiers in Physics, vol. 8, p. 150, 2020. [PubMed: 32509757]

[13]. Wright CJ, Rothwell J, and Saffari N, “Ultrasonic stimulation of peripheral nervous tissue: An investigation into mechanisms,” Journal of Physics: Conference Series, vol. 581, no. 1, p. 012003, 2015.

[14]. Kim H, Taghados S, and Fischer K, “Noninvasive transcranial stimulation of rat abducens nerve by focused ultrasound,” Ultrasound in medicine & biology, vol. 38, no. 9, pp. 1568–1575, 2012. [PubMed: 22763009]

[15]. Downs ME, Lee SA, Yang G, Kim S, Wang Q, and Konofagou EE, “Non-invasive peripheral nerve stimulation via focused ultrasound in vivo,” Physics in Medicine and Biology, vol. 63, no. 3, p. 035011, 1 2018. [PubMed: 29214985]

[16]. Elias WJ, Huss D, Voss T, Loomba J, Khaled M, Zadicario E, Frysinger RC, Sperling SA, Wylie S, Monteith SJ et al., “A pilot study of focused ultrasound thalamotomy for essential tremor,” New England Journal of Medicine, vol. 369, no. 7, pp. 640–648, 2013.

[17]. Legon W, Sato TF, Opitz A, Mueller J, Barbour A, Williams A, and Tyler WJ, “Transcranial focused ultrasound modulates the activity of primary somatosensory cortex in humans,” Nature neuroscience, vol. 17, no. 2, p. 322, 2014. [PubMed: 24413698]

[18]. Lee W, Kim H, Jung Y, Song I-U, Chung YA, and Yoo S-S, “Image-guided transcranial focused ultrasound stimulates human primary somatosensory cortex,” Scientific reports, vol. 5, p. 8743, 2015. [PubMed: 25735418]

[19]. Dickey TC, Tych R, Kliot M, Loeser JD, Pederson K, and Mourad PD, “Intense focused ultrasound can reliably induce sensations in human test subjects in a manner correlated with the density of their mechanoreceptors,” Ultrasound in medicine & biology, vol. 38, no. 1, pp. 85–90, 2012. [PubMed: 22104527]

[20]. Gavrilov L, “Use of focused ultrasound for stimulation of nerve structures,” Ultrasonics, vol. 22, no. 3, pp. 132–138, 1984. [PubMed: 6372189]

[21]. Yoshi B and Lumpkin BHSLEKE, “Focused ultrasound excites action potentials in mammalian peripheral neurons in intact tissue,” PNAS (in review), 2019.

[22]. Wu F, Wang Z-B, Zhu H, Chen W-Z, Zou J-Z, Bai J, Li K-Q, Jin C-B, Xie F-L, and Su H-B, “Feasibility of us-guided high-intensity focused ultrasound treatment in patients with advanced pancreatic cancer: initial experience,” Radiology, vol. 236, no. 3, pp. 1034–1040, 2005. [PubMed: 16055692]

[23]. Treat LH, McDannold N, Vykhodtseva N, Zhang Y, Tam K, and Hynynen K, “Targeted delivery of doxorubicin to the rat brain at therapeutic levels using mri-guided focused ultrasound,” International journal of cancer, vol. 121, no. 4, pp. 901–907, 2007. [PubMed: 17437269]

[24]. Hynynen K, “Mri-guided focused ultrasound treatments,” Ultrasonics, vol. 50, no. 2, pp. 221–229, 2010. [PubMed: 19818981]

[25]. de Bever JT, Odéen H, Hofstetter LW, and Parker DL, “Simultaneous MR thermometry and acoustic radiation force imaging using interleaved acquisition,” Magn. Reson. Med, vol. 79, no. 3, pp. 1515–1524, 3 2018. [PubMed: 28795419]

[26]. Walker WF and Trahey GE, “A Fundamental Limit on Delay Estimation Using Partially Correlated Speckle Signals,” IEEE Trans. Ultrason. Ferroelectr. Freq. Control, vol. 42, no. 2, pp. 301–308, 1995.

[27]. Strasser J, Haindl MT, Stollberger R, Fazekas F, and Ropele S, “Magnetic resonance elastography of the human brain using a multiphase dense acquisition,” Magnetic resonance in medicine, 2019.

[28]. Vappou J, Bour P, Marquet F, Ozenne V, and Quesson B, “MR-ARFI-based method for the quantitative measurement of tissue elasticity: Application for monitoring HIFU therapy,” Phys. Med. Biol, vol. 63, no. 9, p. 095018, 5 2018. [PubMed: 29633958]

[29]. Kaye EA, Chen J, and Pauly KB, “Rapid MR-ARFI method for focal spot localization during focused ultrasound therapy,” Magn. Reson. Med, vol. 65, no. 3, pp. 738–743, 3 2011. [PubMed: 21337406]

[30]. McDannold N and Maier SE, “Magnetic resonance acoustic radiation force imaging,” Med. Phys, vol. 35, no. 8, pp. 3748–3758, 2008. [PubMed: 18777934]

[31]. Gennisson J-L, Deffieux T, Fink M, and Tanter M, “Ultrasound elastography: principles and techniques,” Diagnostic and interventional imaging, vol. 94, no. 5, pp. 487–495, 2013. [PubMed: 23619292]

[32]. Maleke C and Konofagou EE, “In vivo feasibility of real-time monitoring of focused ultrasound surgery (fus) using harmonic motion imaging (hmi),” IEEE Transactions on biomedical Engineering, vol. 57, no. 1, pp. 7–11, 2009. [PubMed: 19643703]

[33]. Lee SY, Cardones AR, Doherty J, Nightingale K, and Palmeri M, “Preliminary results on the feasibility of using arfi/swei to assess cutaneous sclerotic diseases,” Ultrasound in medicine & biology, vol. 41, no. 11, pp. 2806–2819, 2015. [PubMed: 26259888]

[34]. D’hooge J, Heimdal A, Jamal F, Kukulski T, Bijnens B, Rademakers F, Hatle L, Suetens P, and Sutherland GR, “Regional strain and strain rate measurements by cardiac ultrasound: principles, implementation and limitations,” European Journal of Echocardiography, vol. 1, no. 3, pp. 154–170, 2000. [PubMed: 11916589]

[35]. Bihari P, Shelke A, Nwe T, Mularczyk M, Nelson K, Schmandra T, Knez P, and Schmitz-Rixen T, “Strain measurement of abdominal aortic aneurysm with real-time 3d ultrasound speckle tracking,” European Journal of Vascular and Endovascular Surgery, vol. 45, no. 4, pp. 315–323, 2013. [PubMed: 23403222]

[36]. Nightingale K, Stutz D, Bentley R, and Trahey G, “Acoustic radiation force impulse imaging: EX vivo and in vivo demonstration of transient shear wave propagation,” in Proceedings - International Symposium on Biomedical Imaging, vol. 2002-Janua, no. 2. Elsevier, 2 2002, pp. 525–528.

[37]. Nightingale K, “Acoustic Radiation Force Impulse (ARFI) Imaging: A Review,” Current Medical Imaging Reviews, vol. 7, no. 4, pp. 328–339, 11 2011. [PubMed: 22545033]

[38]. Palmeri M, Wang M, Dahl J, Frinkley K, and Nightingale K, “Quantifying Hepatic Shear Modulus In Vivo Using Acoustic Radiation Force,” Ultrasound in Medicine & Biology, vol. 34, no. 4, pp. 546–558, 4 2008. [PubMed: 18222031]

[39]. Pinton GF, Dahl JJ, and Trahey GE, “Rapid tracking of small displacements using ultrasound,” Proceedings - IEEE Ultrasonics Symposium, vol. 4, no. 6, pp. 2062–2065, 2005.

[40]. Han Y, Wang S, Hibshoosh H, Taback B, and Konofagou E, “Tumor characterization and treatment monitoring of postsurgical human breast specimens using harmonic motion imaging (HMI),” Breast Cancer Research, vol. 18, no. 1, p. 46, 2016. [PubMed: 27160778]

[41]. Xia R and Thittai AK, “Real-Time Monitoring of High-Intensity Focused Ultrasound Treatment Using Axial Strain and Axial-Shear Strain Elastograms,” Ultrasound in Medicine and Biology, vol. 40, no. 3, pp. 485–495, 3 2014. [PubMed: 24361216]

[42]. Maleke C and Konofagou EE, “In vivo feasibility of real-time monitoring of focused ultrasound surgery (FUS) using harmonic motion imaging (HMI),” IEEE Transactions on Biomedical Engineering, vol. 57, no. 1, pp. 7–11, 1 2010. [PubMed: 19643703]

[43]. Lee SA, Kamimura HAS, Burgess MT, and Konofagou EE, “Displacement imaging for focused ultrasound peripheral nerve neuromodulation,” IEEE Transactions on Medical Imaging, pp. 1–1, 5 2020. [PubMed: 31135355]

[44]. Jeong JS, Chang JH, and Shung KK, “Ultrasound transducer and system for real-time simultaneous therapy and diagnosis for non-invasive surgery of prostate tissue.” IEEE transactions on ultrasonics, ferroelectrics, and frequency control, vol. 56, no. 9, pp. 1913–22, 9 2009.

[45]. Fink M, Bercoff, and Tanter, “Supersonic Shear Imaging : A New Technique for Soft Tissue Elasticity Mapping,” IEEE transactions on ultrasonics, ferroelectrics, and frequency control, vol. 51, no. 4, pp. 396–409, 2004.

[46]. Luo J and Konofagou E, “A fast normalized cross-correlation calculation method for motion estimation,” IEEE transactions on ultrasonics, ferroelectrics, and frequency control, vol. 57, no. 6, pp. 1347–57, 2010.

[47]. Vappou J, Hou GY, Marquet F, Shahmirzadi D, Grondin J, and Konofagou EE, “Non-contact, ultrasound-based indentation method for measuring elastic properties of biological tissues using harmonic motion imaging (hmi),” Physics in Medicine & Biology, vol. 60, no. 7, p. 2853, 2015. [PubMed: 25776065]

[48]. Han Y, Hou GY, Wang S, and Konofagou E, “High intensity focused ultrasound (HIFU) focal spot localization using harmonic motion imaging (HMI),” Phys. Med. Biol, vol. 60, no. 15, pp. 5911–5924, 8 2015. [PubMed: 26184846]

[49]. Wong DL and Baker CM, “Pain in children: comparison of assessment scales,” Pediatr Nurs, vol. 14, no. 1, pp. 9–17, 1988. [PubMed: 3344163]

[50]. Dhanaliwala AH, Hossack JA, and Mauldin FW, “Assessing and improving acoustic radiation force image quality using a 1.5-D transducer design,” IEEE Trans. Ultrason. Ferroelectr. Freq. Control, vol. 59, no. 7, pp. 1602–1608, 2012. [PubMed: 22828855]

[51]. Shamdasani V and Kim Y, “Two-dimensional autocorrelation method for ultrasound-based strain estimation,” in Annu. Int. Conf. IEEE Eng. Med. Biol. - Proc., vol. 26 II, 2004, pp. 1380–1383.

[52]. Nielsen VK, “Sensory and motor nerve conduction in the median nerve in normal subjects,” Acta Med. Scand, vol. 194, no. 1–6, pp. 435–443, 4 2009.

[53]. Tiran E, Deffieux T, Correia M, Maresca D, Osmanski B-F, Sieu L-A, Bergel A, Cohen I, Pernot M, and Tanter M, “Multiplane wave imaging increases signal-to-noise ratio in ultrafast ultrasound imaging,” Physics in Medicine & Biology, vol. 60, no. 21, p. 8549, 2015. [PubMed: 26487501]

[54]. Blackmore J, Shrivastava S, Sallet J, Butler CR, and Cleveland RO, “Ultrasound Neuromodulation: A Review of Results, Mechanisms and Safety,” pp. 1509–1536, 7 2019.

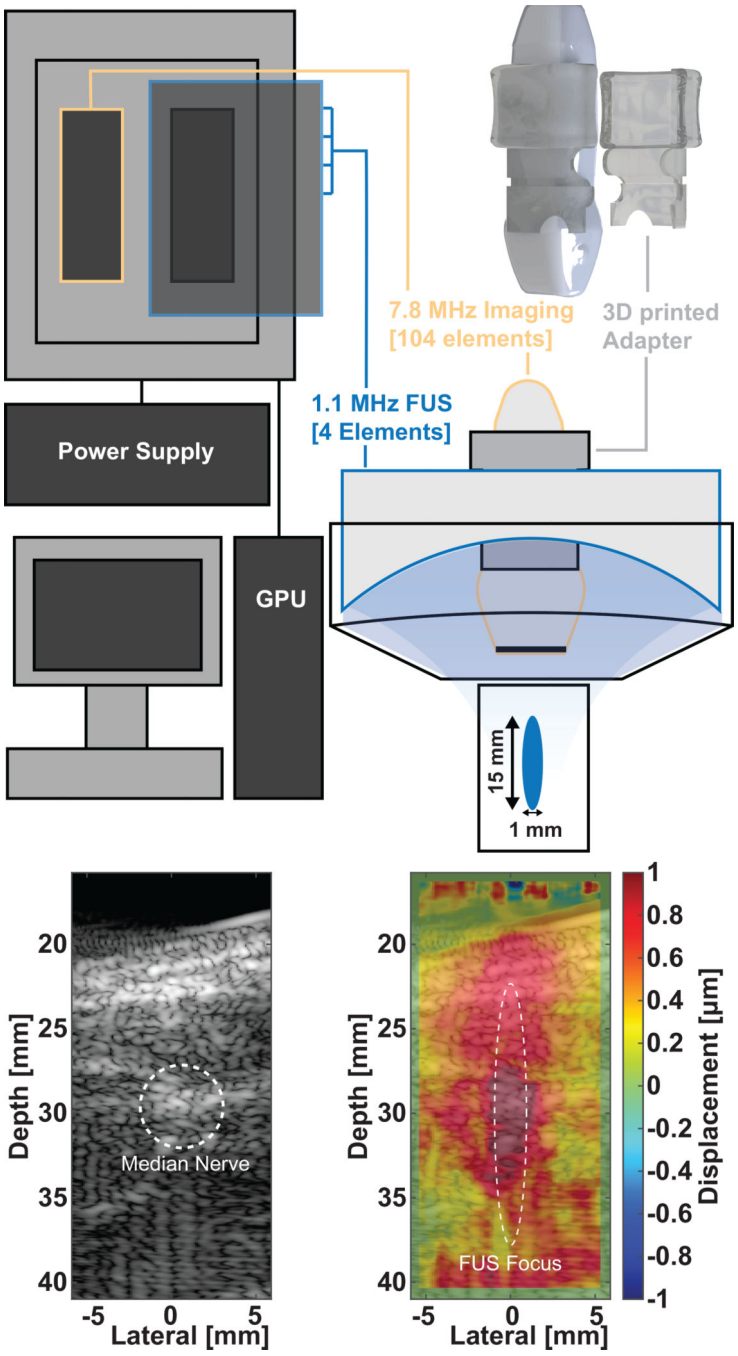


**Fig. 1.**

FUS-imaging Verasonics setup. (top) 256 HIFU vantage with RF matching box and power supply for the 4-element transducer is run using a computer with GPU acceleration. The focal volume and the imaging plane were co-aligned using a 3D printed adapter so that the FUS focal depth (51.74 mm from the rim of the transducer) is centered at 30 mm in the imaging window. (bottom) Compounded plane-wave B-mode images were used to first identify the nerve. Then displacement tracking during FUS propagation was used to confirm FUS delivery in real-time.

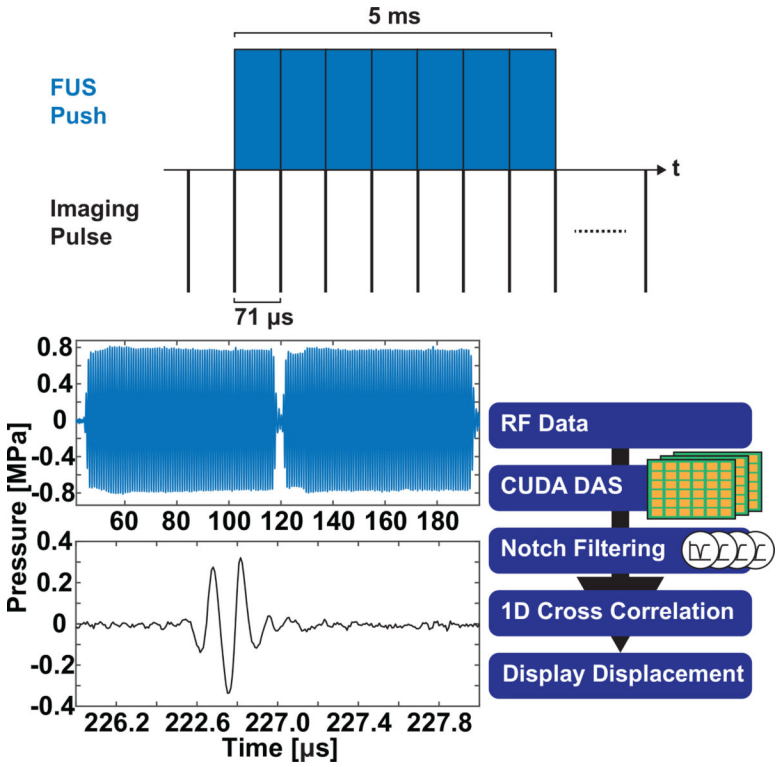


**Fig. 2.**

Within-FUS pulse sequence as recorded using a hydrophone in free-field. The FUS pulse is displayed in blue (acquired with a HFO-660 hydrophone), and the imaging pulse is displayed in black (acquired with a HGL-200 hydrophone). Flow diagram of whole DAQ sequence is shown on the right.

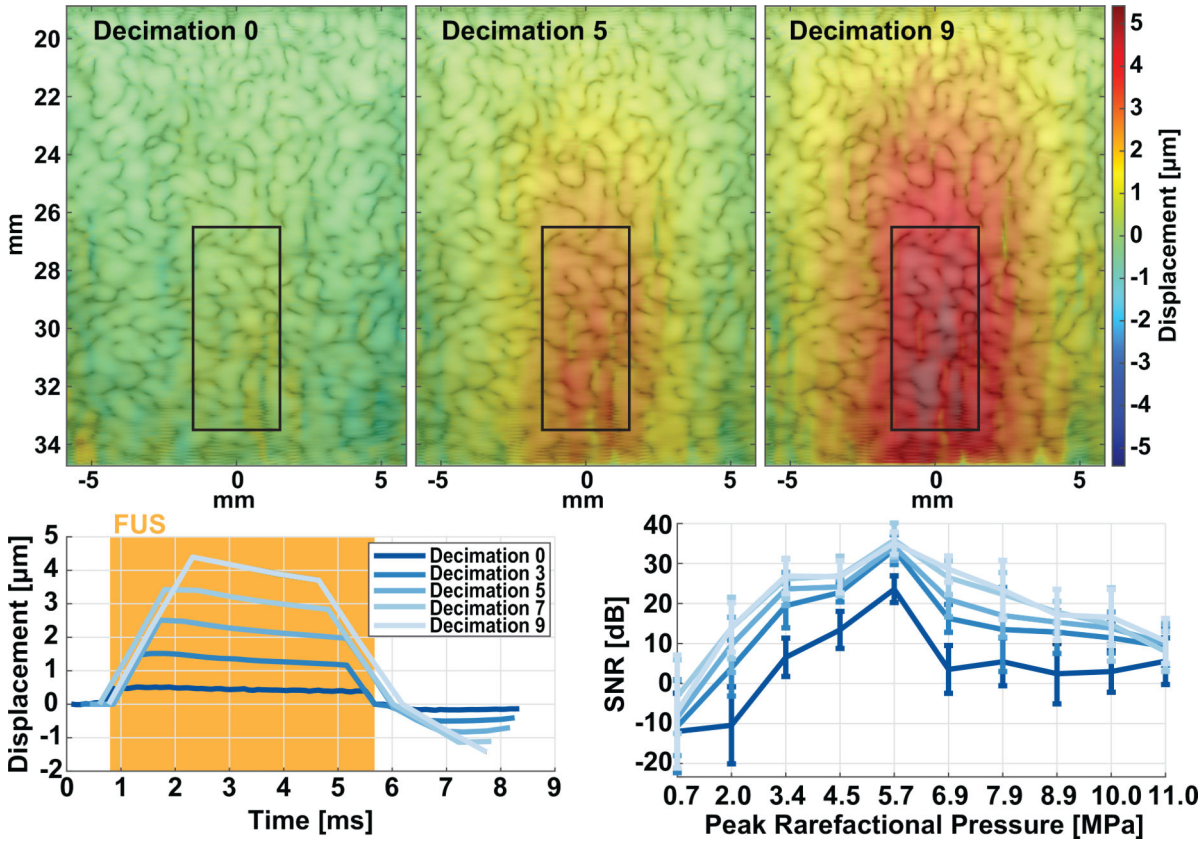


**Fig. 3.**

Displacement tracking for decimation by 0, 3, 5, 7, and 9 frames in a tissue mimicking phantom. Top shows interframe displacement maps for 0, 5, and 9 frame decimation. Bottom shows representative interframe displacement traces from the same RF data after decimation and corresponding SNR calculations over pressures between 0.7 to 11 MPa peak negative.

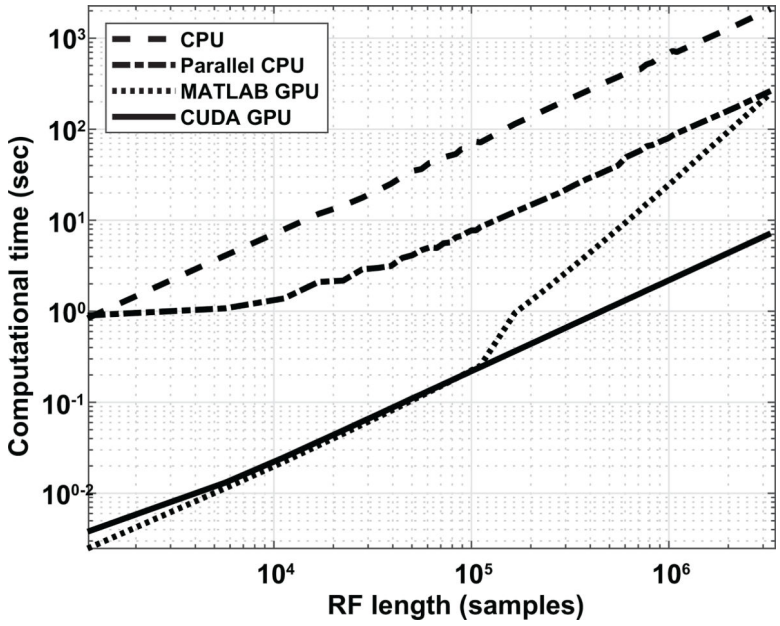


**Fig. 4.**

Log plot of DAS computational time of CPU, parallel CPU, MATLAB GPU parallel computing toolbox, and CUDA GPU over RF length.

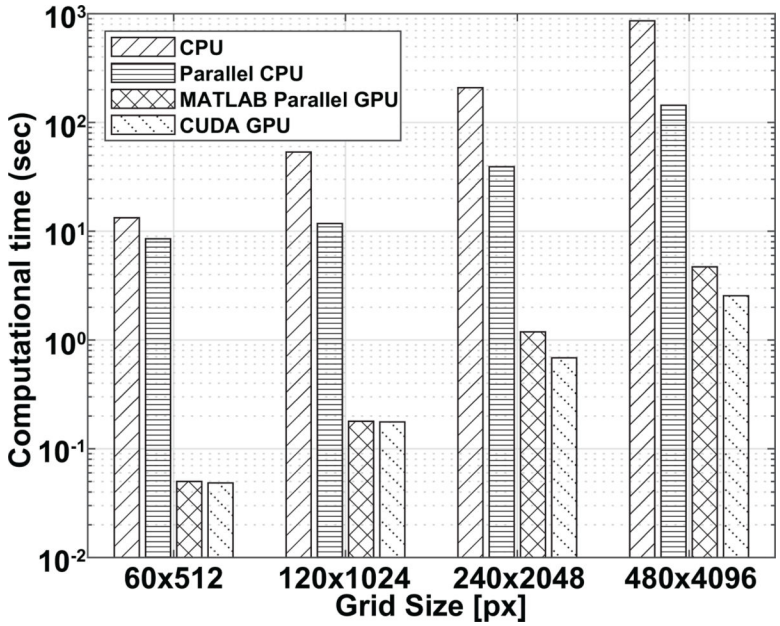


**Fig. 5.**

Computational time for CPU, parallel CPU, MATLAB parallel GPU, and CUDA GPU operations for increasing interpolated grid sizes for DAS beamforming. Computational time is expressed in log scale.

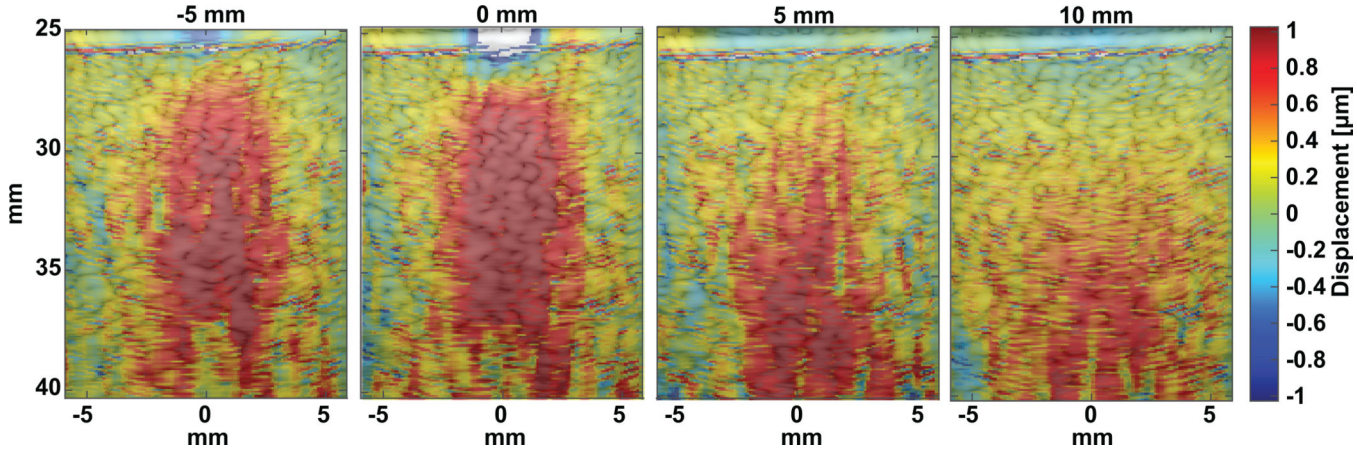


**Fig. 6.**

Displacement maps produced using a gelatin tissue-mimicking phantom at −5, 0, 5, and 10 mm focal depths. Frames shown are at the peak interframe displacement for a 5 ms FUS push.

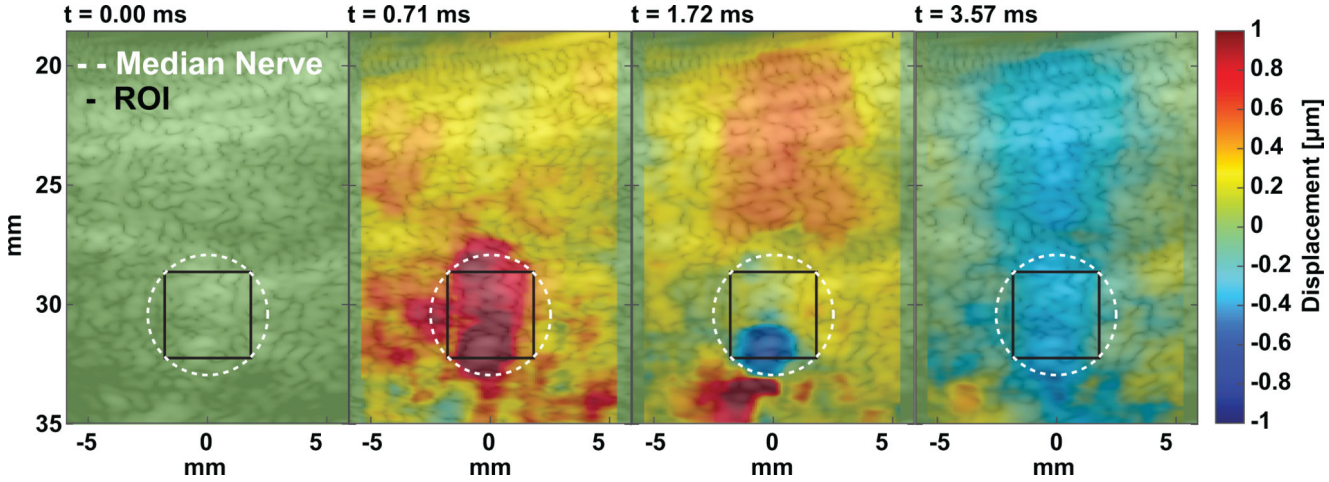


**Fig. 7.**

Representative tracked displacements before, during, and after FUS push in the human subject forearms. The Median nerve is outlined and centered at 30 mm. The median nerve was outlined based on B-mode images where the center of the nerve was identified and an area of 19.6 $mm^2$ was selected encompassing a radius of 2.5 mm that corresponds to the cross-sectional diameter of the median nerve.

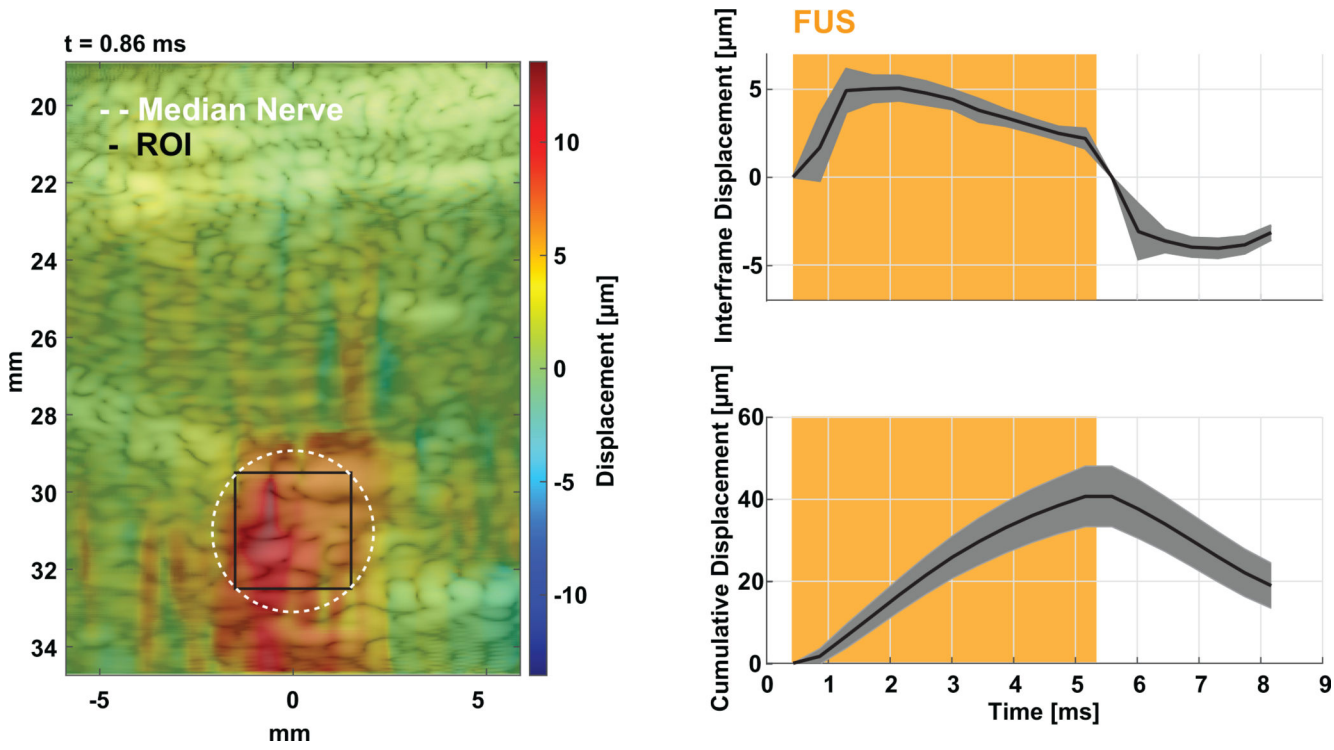


**Fig. 8.**

Illustration of targeting and monitoring FUS neuromodulation using simultaneous displacement imaging. Left shows a displacement map at 0.86 ms after triggering the FUS pulse. The median nerve is located at a depth of approximately 31 mm and was outlined based on B-mode images using an area of 19.6 $mm^2$. Right shows average and standard deviation interframe and cumulative displacement traces over 7 FUS on-target stimulations from the ROI shown in black.

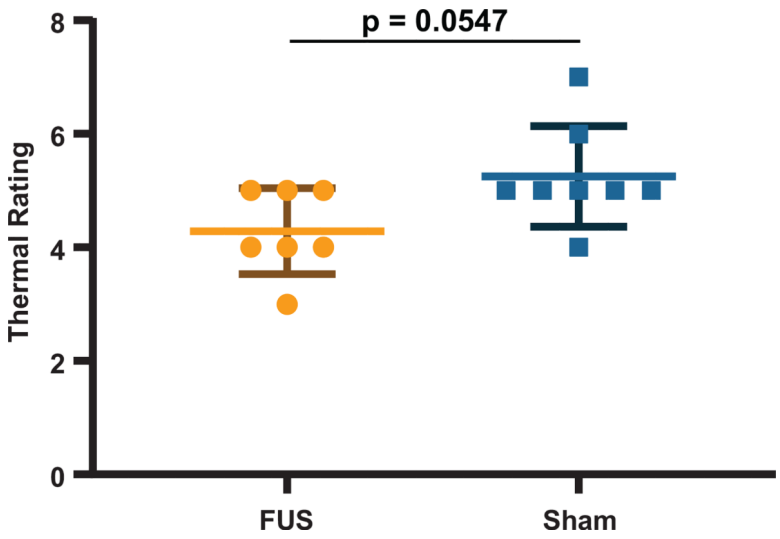


**Fig. 9.**

Thermal ratings for heat pulses with FUS and sham treatment to the median nerve ($p$ = 0.0547, two-tailed unpaired Mann-Whitney test)

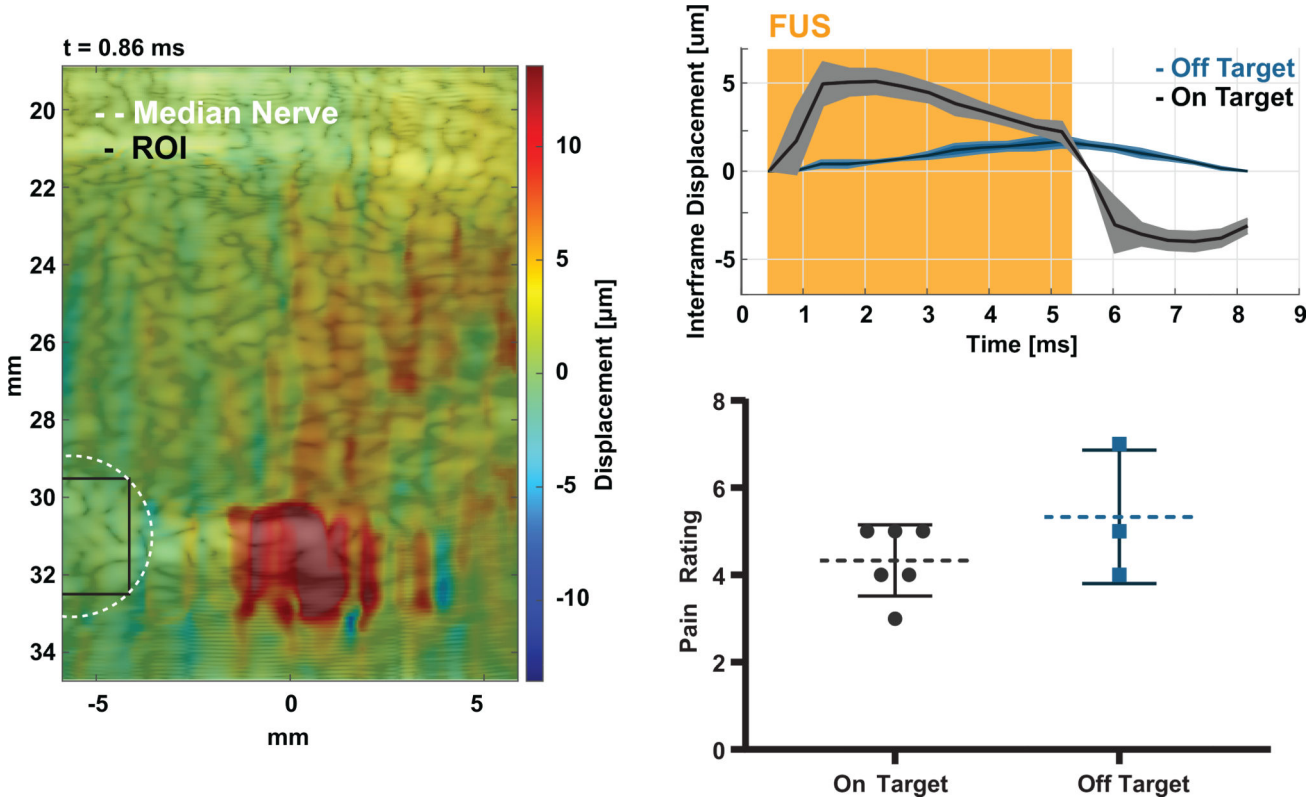


**Fig. 10.**

Representative off-target stimulation. Left shows the displacement map for a FUS pulse where the nerve was located 5 mm laterally from the FUS focus (off target). Right shows the interframe displacement at the ROI on the nerve for on- vs off-target stimulations and corresponding thermal ratings for each trace.

**TABLE I**

Summary of measured displacements across subjects.

| Subject | Pressure [MPa] | Interframe displacement [$\mu$m] | Cumulative displacement [$\mu$m] |
|---|---|---|---|
| **1** | 5.6 | 2.1±0.3 | 18.3±2.4 |
| **2** | 5.6 | 5.5±0.3 | 50.1±3.4 |
| **3** | 7.9 | 4.2±0.3 | 31.3±2.3 |
| **4** | 7.9 | 5.2±0.5 | 42.3±5.5 |
| **5** | 7.9 | 5.1±1.6 | 40.7±10.7 |